Solid State Communications 152 (2012) 1331–1340

Contents lists available at SciVerse ScienceDirect

Solid State Communications

journal homepage: www.elsevier.com/locate/ssc

Thermal properties of graphene and multilayer graphene: Applications in thermal interface materials

Khan M.F. Shahil [1], Alexander A. Balandin *

Nano-Device Laboratory, Department of Electrical Engineering and Materials Science and Engineering Program, Bourns College of Engineering, University of California – Riverside, Riverside, CA 92521, USA

ARTICLE INFO

Article history:
Accepted 12 April 2012
Accepted by L. Bery
Available online 25 April 2012

Keywords:
A. Graphene
A. Thermal interface materials
C. Graphene composites
D. Thermal properties

ABSTRACT

We review the thermal properties of graphene and multilayer graphene, and discuss graphene's applications in thermal management of advanced electronics and optoelectronics. A special attention is paid to the use of the liquid-phase-exfoliated graphene and multilayer graphene as the fillers in the thermal interface materials. It has been demonstrated that addition of an optimized mixture of graphene and multilayer graphene to the composites with different matrix materials produces the record-high enhancement of the effective thermal conductivity at the small filler loading fraction ($f \leq 10$ vol%). The thermal conductivity enhancement due to the presence of graphene in the composites has been observed for a range of matrix materials used by industry. The hybrid composites where graphene is utilized together with metallic micro- and nanoparticles allow one to tune both the thermal and electrical conductivity of these materials. Theoretical considerations indicate that the graphene-based thermal interface materials can outperform those with carbon nanotubes, metal nanoparticles and other fillers owing to graphene's geometry, mechanical flexibility and lower Kapitza resistance at the graphene–base material interface.

1. Introduction: terminology and motivations

We start the discussion of thermal properties of graphene and multilayer graphene (MLG) and their application in thermal management by defining the terminology. It is often problematic to distinguish between MLG and graphite films or between MLG and graphite nano-platelets (GnP). The definition of graphene – a single atomic plane of sp^2-bound carbon – is strict and clear. The distinction between MLG and thin film of graphite or bulk graphite is more obscure and can depend on the context as well as particular application. Some authors, who focus on electrical properties, consider the material to be MLG rather than graphite as long as it is thin enough to have its carrier density tuned via the electrostatic gating, e.g., in the field-effect transistor type structures. In the thermal context, it is reasonable to consider the film to be MLG as opposed to graphite as long as its Raman spectrum is distinctively different from that of bulk graphite. The thermal properties of graphene and graphite at room temperature (RT) are dominated by the acoustic phonons [1]. The optical phonons determine the Raman spectrum. In both cases it is the crystal lattice dynamics that defines the difference between MLG and graphite. The Raman spectrum of MLG is different from that of bulk graphite until the thickness H of approximately 7–10 atomic planes is reached [2–8]. Thus, we consider the materials to be MLG when its lattice dynamic – phonon – properties are different from those of graphite ($H \leq 10 \approx 3.5$ nm). It is also assumed that MLG have much larger lateral dimensions (up to a few micrometers) than their thickness H. The GnP terminology implies nano-particles made from graphite, which can have much thicker than MLG. In addition, the lateral dimensions of GnP can be of the same order of magnitude as the thickness, i.e., the aspect ratio can be close to one. These factors determine the differences in thermal properties between MLG and GnP.

The initial interest to the thermal properties of graphene and MLG was driven by the exotic physics of two-dimensional (2D) phonon transport [1]. However, recently there was a strong motivation to investigate thermal properties of graphene and related composite materials from the positions of practical applications. In this review, we briefly outline the experimental and theoretical works on thermal properties of graphene, summarize the state-of-the-art in this field, and spend more time on discussion of thermal properties of graphene-based composites and practical applications of graphene and MLG for thermal management. The readers interested in fundamentals of the phonon heat conduction in graphene and MLG are referred to other comprehensive reviewers [1,8].

Rapidly increasing power densities in electronics made efficient heat removal a crucial issue for progress in information, communication and energy storage technologies [9,10]. Development of the

* Corresponding author.
E-mail address: balandin@ee.ucr.edu (A.A. Balandin).
URL: http://ndl.ee.ucr.edu/ (A.A. Balandin).
[1] Present address (KMFS): Intel Corporation, Hillsboro, OR 97124, USA.

0038-1098/$ - see front matter © 2012 Elsevier Ltd. All rights reserved.
http://dx.doi.org/10.1016/j.ssc.2012.04.034

next generations of integrated circuits (ICs), three-dimensional (3D) integration and ultra-fast high-power density transistors makes the thermal management requirements extremely severe [9–14]. Efficient heat removal became a critical issue for the performance and reliability of modern electronic, optoelectronic, photonic devices and systems. The thermal interface materials (TIMs), applied between heat sources and heat sinks, are essential ingredients of thermal management [10–14]. Conventional TIMs filled with thermally conductive particles require high volume fractions f of filler ($f\sim50\%$) to achieve thermal conductivity K of the composite in the range of $\sim$1–5 W/mK at room temperature (RT) [11–14].

The demands for better TIMs are not limited to electronics used in information processing and communications. The key power generation technologies for the ongoing "green" revolution – photovoltaic (PV) solar cells – also require efficient thermal management. The solar cells are based on various materials, including crystalline Si and conjugated polymers [15,16]. The state-of-the-art PV solar cells have efficiency of about 15% in converting absorbed light into electricity [17]. Absorbing light, PV cells convert about 70% of solar energy into heat. This heat must be efficiently removed from the cell to prevent degradation of performance or damage to the cell. The temperature rise degrades the power conversion efficiency in PV cells approximately linearly with the coefficient of 0.23 W/°C in the temperature range from 25 °C to 70 °C for crystalline Si [15]. This corresponds to $\sim$20% reduction in produced power due to thermal build-up. Other studies have identified $\sim$0.5% efficiency loss per 1 °C increase in the cell temperature [18]. Considering that the highest temperatures of PV solar panels are $\sim$70 °C, the overall efficiency loss can be very significant [19]. It was observed that a reduction in the PV cell temperature by 15 °C at one sun illumination boosts $\sim$6% in the output power [17,20]. These facts explain why TIMs with high thermal conductivity and low thermal contact resistance with pertinent solids, e.g., semiconductors or metals, are essential for further progress in PV energy conversion.

In this review we focus our attention on graphene's use in TIMs. We describe composites with an optimized mixture of graphene [21] and multilayer graphene (MLG), produced by high-yield liquid-phase-exfoliation (LPE) technique [22–24], with the strongly enhanced cross-plane thermal conductivity K. It is demonstrated that one can significantly improve the heat conduction properties of the commercial TIMs with a small addition ($f\sim2\%$) of the graphene–MGL filler following a proper technology. We note here that the demonstrated enhancement of TIMs' thermal conductivity by a factor of 10–20 compared to that of the matrix materials may lead to revolutionary increase in device and system performance not only in electronics but also in optoelectronics and renewable energy generation.

2. Basics of thermal interface materials

Since the primary purpose of this review is to analyze graphene in the context of practical applications we describe the basics of TIMs in some details. The function of TIMs is to fill the voids and grooves created by imperfect surface finish of two mating surfaces (Fig. 1(a) and (b)), thus forcing air out and improving surface contact and the conduction pathway across the interface (Fig. 1(b)). Fig. 1(a) shows a typical packaging architecture for desktop computers used for real electronic cooling applications. Two TIM layers are used to ensure a continuous path for the heat flow. The first layer – inserted between the backside of the device and the integrated heat spreader (IHS) lid – is conventionally termed TIM-1 while the second TIM layer – termed TIM-2 – is used between IHS and the heat sink (Fig. 1(a)).

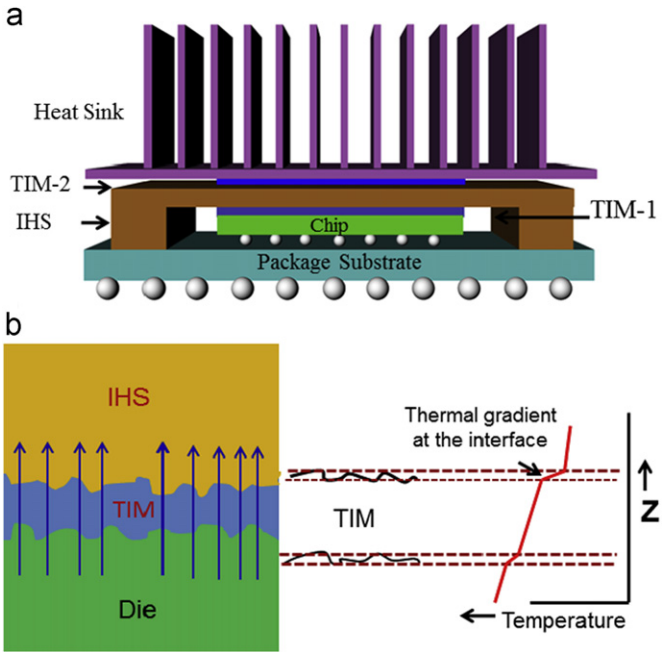

Fig. 1. (Colr online) Schematic of the action of the thermal interface material, which fills the gaps between two contacting surfaces. The heat removal improves with the higher thermal conductivity, smaller bond line thickness and smaller contact resistance of TIMs with the surfaces.

TIMs' performance is characterized by $R_{TIM}=BLT/K+R_{C1}+R_{C2}$, where BLT is the bond line thickness and $R_{C1,2}$ are the TIM's contact resistance with the two bounding surfaces. The magnitude of R_{TIM} depends on the surface roughness, interface pressure P, temperature T, and viscosity ξ. The common TIMs are composites, which consist of polymer matrix or base material and thermally conductive filler particles. TIMs have to be mechanical stabile, reliable, non-toxic, low-cost and easy to apply [10–14]. They should possess as high K as possible, as well as low ξ and coefficient of thermal expansion. The industrial TIMs have R_{TIM} $\sim3–10\times10^{-6}$ K m^2/W [11]. The drive to reduce size L of the conventional fillers, e.g., metal particles, is explained by the fact that smaller L at high f results in larger particle-to-particle contact area and lower R_{TIM} [14]. Recently, there were strong efforts in industry to further reduce R_{TIM}. The latter is explained not only by the increasing dissipated total power Q but also by the strongly non-uniform heat flux distribution within the chip [25,26]. The problem of thermal management of the chip includes two tasks: maintaining the average temperature of the chip below a certain design point and keeping the temperature of the hottest spot below a certain level. Improved TIMs can help to accomplish both tasks.

The efficiency of the filler in TIMs is characterized by the thermal conductivity enhancement (TCE) defined as $\eta=(K-K_m)/K_m$, where K is thermal conductivity of the composite and K_m is thermal conductivity of the matrix material. TCE of $\sim$170% at the 50% loading of conventional fillers such as silver or alumina with the filler particle size $L<10$ μm are considered to be standard. Apart from the thermal requirements, the specific needs for the electrical insulation of electronic components have considerable impacts on the product design-in of thermal interface materials. TIMs therefore can be classified into the electrically insulating (e.g., silicone foils, engineering plastics, phase change films) and the electrically conductive materials (e.g., thermal grease). In addition, parameters such as chemical stability, proper surface properties with minimal surface deviations, mechanical tolerances, softness and flexibility, tensile strength, easy handling and

last but not least the economic efficiency have to be considered to meet the industry requirements. The environmental compatibility, suitability to adhesive, chemical, temperature and ageing resistance, as well as lifetime are other important factors. These requirements limit the type of materials and nanostructures, which can be used as fillers in TIMs. They also explain a strong interest to each new material with excellent thermal properties from the TIM application prospective.

Some time ago, CNTs attracted attention as highly thermally conductive fillers for TIMs. Their main attractive feature is extremely high intrinsic thermal conductivity K_i of CNTs in the range of ~3000–3500 W/mK at RT [27,28]. The outcomes of experiments with CNT-based TIMs were controversial. The measured TCE factors were moderate, in the range ~50–250% at f~7% of the CNT loading [29–31]. In some cases, K was not improved substantially [30] or even decreased with addition of single-wall CNTs [32]. The common reason offered as an explanation was that although CNTs have excellent K_i they do not couple well to the matrix material or contact surface. The reported thermal boundary resistance (TBR) between CNTs and polymer matrix was as high as $\sim 10^{-7}$ m^2 K/W [33]. The large TBR at CNT–matrix interface can be attributed to the fundamental property—high Kapitza resistance [34] between one-dimensional (1D) CNTs and 3D bulk owing to the large difference in the phonon density of states (DOS). It was also suggested that the lack of thermal percolation in CNT composites can negatively affect their heat conduction properties [35]. Interestingly, the electrical percolation thresholds f_T for CNT composites are very low, f~0.1 vol%, compared to 20–30 vol% for composites with spherical fillers [14,35]. TIMs with aligned CNTs have better K but suffer from large R_C and prohibitive cost. These outcomes provided strong motivation for the search of alternative high-K fillers and stimulated interest to graphene and multi-layer graphene as fillers for TIMs.

3. Intrinsic thermal conductivity of graphene

In 2008, it was discovered that graphene has extremely high intrinsic K_i, which exceeds that of CNTs [1,36–38]. The latter was confirmed by theoretical studies [1,37,38]. MLG retains excellent thermal properties [1,38]. Graphite, which is 3D bulk limit for MLG with the number of layers $n \to \infty$, is still an outstanding heat conductor with the intrinsic $K_i \approx 2000$ W/mK at RT. For comparison, $K_i \approx 430$ W/mK for silver and it is much lower for silver nanoparticles used in TIMs. The first experimental studies of thermal conductivity of graphene were carried out at UC Riverside [1,36,38–40] using an original non-contact Raman optothermal technique (see Fig. 2(a)). The measurements were performed with large-area suspended graphene layers exfoliated from high-quality bulk graphite. The development of the optothermal technique was essential for performing the thermal measurements with the atomically thin materials. It was found that the thermal conductivity K can exceed ~3000 W/mK near RT for sufficiently large graphene flakes. The measured thermal conductivity of graphene was above the bulk graphite limit. The phonon mean-free path (MFP) was estimated to be ~775 nm near RT [39].

In the Raman optothermal technique, the heating power ΔP is provided with the laser light focused on a suspended graphene layer connected to heat sinks at its ends. Fig. 2(b) shows an example of the sample for the Raman optothermal measurements, which is a few-layer graphene (FLG) ribbon of rectangular shape with the number of atomic planes $n=2$ suspended across a 3-μm-wide trench in Si wafer. The temperature rise ΔT in response to the dissipated power ΔP is determined with a micro-Raman spectrometer. The Raman G peak in graphene's Raman spectrum exhibits strong temperature T dependence. The calibration of the spectral position of G peak with temperature has to be performed by changing the sample temperature while using very low laser power to avoid local heating. The calibration curve allows one to convert a Raman spectrometer into an "optical thermometer".

During the thermal conductivity measurements the suspended graphene layer is heated by the increasing laser power. The local temperature rise in graphene is measured as $\Delta T = \Delta\omega_G/\zeta_G$, where ζ_G is the temperature coefficient of the Raman G peak in the relevant temperature range [1]. The amount of heat dissipated in graphene can be determined either via measuring the integrated Raman intensity of G peak, as in the original experiments [36], or by a detector placed under the graphene layer, as in the follow up experiments [41]. Since the optical absorption in graphene depends on the light wavelength [42] and can be affected by strain, defects, contaminations and near-field or multiple reflection effects for graphene flakes suspended over the trenches, it is essential to measure absorption under the conditions of the experiment. The relatively strong dependence of the light absorption in graphene on the wavelength results from the many-body effects [42].

A correlation between ΔT and ΔP for graphene samples with a given geometry gives the thermal conductivity value via solution of the heat diffusion equation. The suspended portion of graphene is essential for determining ΔP, forming two-dimensional heat front propagating toward the heat sinks, and reducing thermal coupling to the substrate. The method also allows one to monitor temperature of Si and SiO_2 layer near the trench with suspended graphene from the shift in the position of Si and SiO_2 Raman peaks. This can be used to ensure and monitor the weak thermal coupling of graphene to SiO_2 insulating layer. The thermal conductivity data in the Raman optothermal technique can be extracted for the graphene and MLG flakes of arbitrary shape via the iterative solution of the heat-diffusion equation using the finite element method [38].

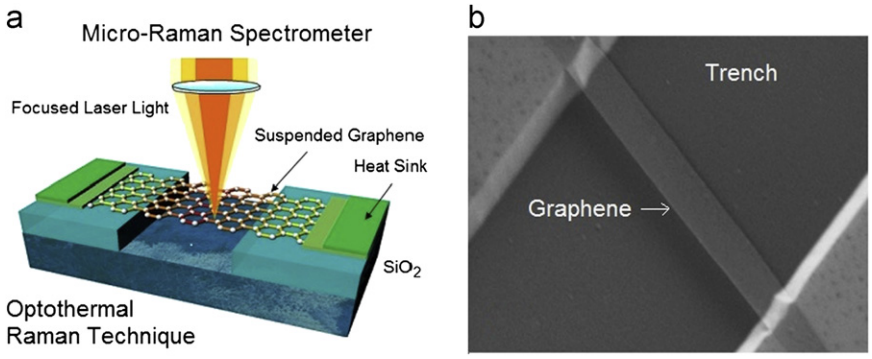

Fig. 2. (Color online) (a) Illustration of the optothermal Raman technique used for the first measurements of the thermal conductivity of graphene. (b) SEM image of FLG with $n=2$ of rectangular shape suspended across a 3-μm-wide trench in a Si wafer for the thermal measurements.

Independent studies conducted by other research groups [41] also utilized the non-contact Raman optical technique but modified it via addition of a power meter under the suspended portion of graphene. The latter was made possible via utilization of the suspended samples fabricated in the form of membranes. It was found that thermal conductivity of the suspended high-quality CVD graphene exceeded ~2500 W/mK at 350 K, and it was as high as $K \approx 1400$ W/mK at 500 K [41]. The reported value is larger than thermal conductivity of bulk graphite at RT, which is about ~2000 W/mK. Other optothermal studies with suspended graphene found thermal conductivity in the range from ~1500 to ~5000 W/mK [43].

The data for suspended or partially suspended graphene is closer to the intrinsic thermal conductivity because suspension reduces thermal coupling to the substrate and scattering on the substrate defects and impurities. For practical applications, it is also important to know in-plane and cross-plane thermal conductivity of supported graphene, i.e., graphene attached to the substrate along its entire length. The measurements for exfoliated graphene on SiO_2/Si revealed in-plane $K \approx 600$ W/mK near RT [44]. This value is below those reported for suspended graphene but it is still rather high exceeding thermal conductivity of Si and copper. In Ref. [44] the authors calculated the theoretical thermal conductivity of free graphene to be ~3000 W/mK near RT. The reduced experimental of the thermal conductivity of graphene on a substrate was attributed to the graphene–substrate coupling. Detail description of thermal conductivity measurements and comparison of the results among different groups was provided in Ref. [1].

4. Preparation of graphene-based thermal interface materials

The earliest graphene samples were produced using the micro-mechanical cleavage [21]. Recently the efforts have been focused on developing large scale methods of graphene production [22–24,45–47]. The electronic applications require high-quality graphene. The most promising approach for this type of applications is chemical vapor deposition (CVD) [48–51]. The thermal management applications cannot become practical without a large-scale inexpensive production of graphene, which can be of a lower grade. Graphene's liquid-phase exfoliation using various solvents shows most promise for this purpose.

The surfactant stabilized graphene dispersion method [22–24] and graphene composite preparation techniques [52,53] were adopted for testing graphene as the TIM filler. These approaches require relatively little chemical and thermal treatments and allows one to produce sufficient quantities of TIMs for detail study (Fig. 3). In this section and below we outline LPE and TIM synthesis processes following description in Ref. [54]. The dispersions were prepared by ultrasonication of graphite flakes in aqueous solution of sodium cholate followed by sonication and centrifugation. The graphene–MLG nanocomposites were prepared by ultrasonication (~10–12 h) of natural graphite in aqueous solution of sodium cholate. The solution was left for ~1 h to settle followed by removal of thick graphite flakes. The ultrasonicated solution underwent sedimentation processing in a centrifuge. The centrifugation was performed at 15k rpm for 5 min. After centrifugation the top layer was decanted and dried in a vacuum oven. It was again dispersed in water by the high-sheer mixing followed by ultrasonication for ~2 h. The solvent was dried at 60 °C in a vacuum oven leaving graphene and MLG consisting of 1–10 stacked atomic monolayers. The epoxy resin was added to the suspension following an in-house developed procedure (see Ref. [54] and its Supplemental Information). The curing agent was added under continuous stirring in a ratio of epoxy to curing agent of 100:26 by weight. The homogeneous mixture of epoxy and graphene–MLG nanocomposite was loaded into a custom stainless steel mold, heated and degassed in vacuum for curing. The composites were cured at 100 °C for 2 h and at 150 °C for additional 2 h to complete the curing cycle. The samples were prepared with different graphene loadings varying between 1 and 10% of volume fraction. In the trial-and-error procedure the optimum sonication time t_s and centrifugation rate r_c resulting in the largest η were determined.

Fig. 3(a)–(f) presents a schematic of the preparation procedure of the graphene-based composites for TIM applications as well as representative characterization data. The LPE produced graphene

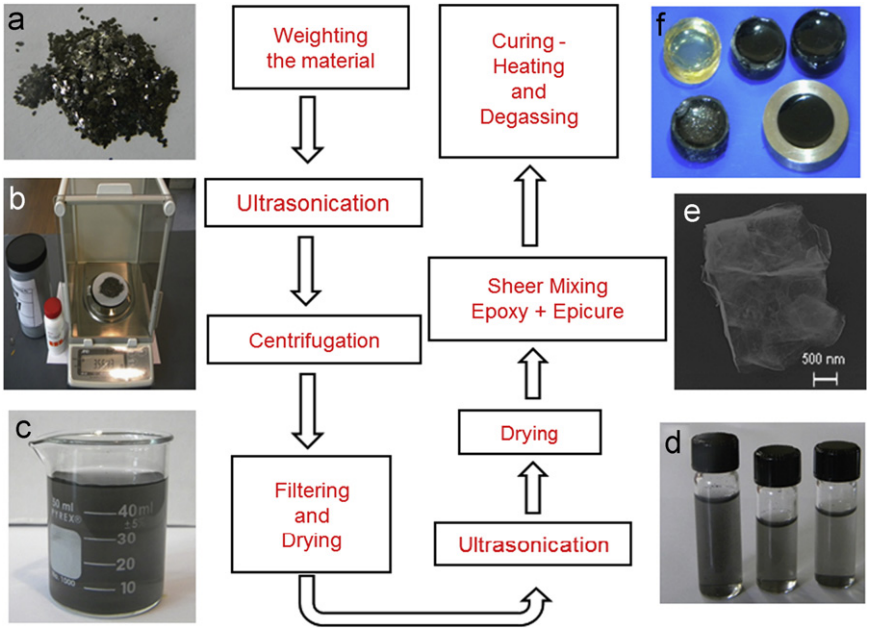

Fig. 3. (Color online) Schematic of the preparation process of the graphene–MLG polymer nanocomposite TIMs: (a) graphite source material; (b) weighting the utilized materials—natural graphite and sodium cholate; (c) graphene solution after the first ultrasonication and centrifugation; (d) LPE graphene dispersion at different concentration; (e) SEM image of MLG revealing overlapping regions and wrinkles, which improve thermal coupling; (f) optical image of graphene–MLG polymer composite samples prepared for thermal measurements.

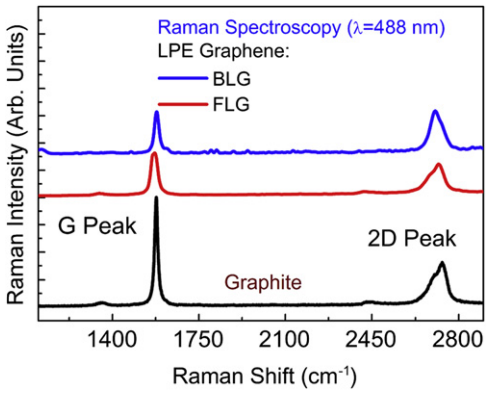

Fig. 4. (Color online) Raman spectroscopy image of bilayer graphene and MLG flakes extracted from the solution. The presence of the single layer, bilayer graphene and MLG with $n<5$ was essential for the observed thermal conductivity enhancement.

and MLG were characterized using the optical, scanning electron microscopy (SEM) and atomic force microscopy (AFM) techniques. The thickness H ($=h\times n$, where $h=0.35$ nm is the thickness of a graphene monolayer) and size L distribution of MLG in the nanocomposites were important for maximizing η. Extremely small dimensions of the resulting graphene sheet led to the wrinkled topology at the nanoscale as shown in Fig. 3(e). The nanoscale surface roughness of FLG could play an important role in enhancing mechanical interlocking and load transfer with the matrix and consequently, better adhesion [52].

The micro-Raman spectroscopy was used to verify n [6]. The n counting with the Raman spectroscopy is efficient for $n<7$. For thicker flakes the thickness distribution statistics was also derived from AFM inspection. Fig. 4 shows an example of Raman spectra of MLG from the solution and the reference graphite source excited at $\lambda=488$ nm. Deconvolution of 2D band and comparison of the I(G)/I(2D) intensity ratio allowed us to determine n with a high accuracy, e.g., the plotted spectra correspond to the large-size bilayer graphene ($n=2$) and MLG with $n\approx 5$ with. The weak intensity of the disorder D peak indicates the large lateral size and low defect concentration (the diameter of the laser spot in the micro-Raman spectroscopy was $\sim$1 μm).

The graphene–MLG concentrations utilized for preparation of the nanocomposite TIMs were $\sim$0.253 mg/mL ($t_s\approx 12$ h, $r_c=15$k rpm). It was established that the composites with $\sim$10–15% of MLG with $n\leq 2$, $\sim$50% of FLG with $n\leq 5$ are the optimum for maximizing η. Based on the optical microscopy and SEM examination, most of the graphene and MLG flakes ($\sim$90%) had lateral dimensions in the range $L\approx 50$ nm–0.5 μm. A small fraction of the flakes ($\sim$10%), predominantly with $n<5$, had large lateral sizes $L\approx 2$–5 μm. As discussed below, their presence in the TIM composites was important. The prepared nanocomposite graphene–MLG solutions were mixed with epoxy followed by curing and heating in vacuum to produce a large number of samples with the carbon loading $f\sim$0.2–10 vol%.

5. Thermal properties of graphene-based TIMs

Thermal conductivity measurements were conducted with the "laser flash" technique. In the laser flash method, for a given geometry of the samples, heat propagates from the top to the bottom surface of the material under test. It means that the measured K is more closely related to the cross-plane, also referred to as through plane, component of the thermal conductivity tensor. The cross-plane K is the one, which is important for TIMs' performance. The sample thicknesses were 1–1.5 mm to ensure that their thermal resistances were much larger than the contact resistance. All measurements reported in Ref. [54] started with the control experiments—measurements of the thermal conductivity of pristine epoxy. The obtained values for the pristine epoxy were $K=0.201$ W/mK at RT (in agreement with the epoxy vendor's specifications).

Fig. 5 shows TCE factor as a function of the loading fraction of filler f for the graphene–MLG-nanocomposite epoxy—sample A ($t_s\approx 12$ h, $r_c=15$k rpm) and sample B ($t_s\approx 10$ h, $r_c=5$k rpm) at RT. For comparison, TCE for the epoxy composites with graphite micro- and nanoparticles obtained by grinding of graphite (substantial fraction of particles have $L\sim 40$ μm) and TEC for the epoxy composite with commercial carbon black (CB) powder are also shown. One can see that there is a very large increase in η for the graphene–MLG nanocomposites. At $f=10$ vol% loading, K reaches the value of $\sim$5.1 W/mK, which corresponds to TCE of $\sim$2300%. Traditional fillers with small aspect ratios show TCE $\sim$20% per 1 vol% loading. The measured TCE for composites with the amorphous graphite particles were low and consistent with the literature [10–14]. The control experiments with graphite particles and CB confirm that the thermal properties of graphene and MLG are essential for increasing the thermal conductivity of TIMs [54].

It is interesting to note that TCE follows approximately linear dependence on f without revealing any clear signature of thermal percolation threshold. One would expect to observe a kink in $K(f)$ plot and $K=K_T[(f-f_T)/(1-f_T)]^{\beta}$ dependence (where $\beta\approx 2$ in 3D) if the percolation is resolved. The physics of the thermal percolation is still a subject of debates [10,30,35,52]. Unlike electrical percolation, the thermal percolation threshold can be less pronounced due to heat conduction by the matrix. Fig. 6 shows the thermal conductivity as a function of temperature for different loading f. The thermal conductivity decrease with temperature at higher loading can be related to the Umklapp phonon scattering characteristic for crystalline materials. This suggests that heat is carried by the thermally linked graphene or MLG flakes when $f\sim$10%. Contrary, in pristine epoxy the $K(T)$ dependence is nearly absent, which is expected for the non-crystalline amorphous solids [1]. The temperature dependence of our graphene TIMs is still rather weak, which is beneficial for the thermal management applications.

To rationalize the experimental data, one can use the Maxwell–Garnett effective medium approximation (EMA), which works well for $f<40\%$ [55,56]. In Ref. [54] it was modified to include the size of the fillers, aspect ratios α and TBR between the fillers and matrix.

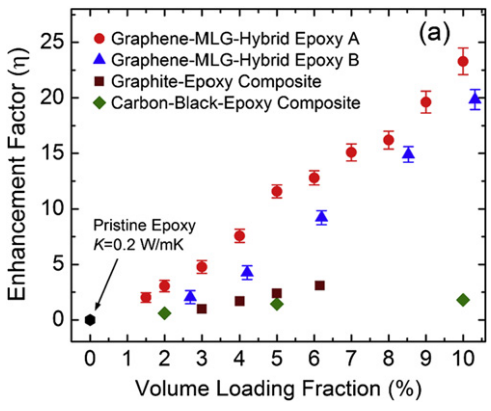

Fig. 5. (Color online) Thermal conductivity enhancement in the graphene–MLG-nanocomposite epoxy TIMs as a function of the filler volume loading fraction. Note an extremely large enhancement by a factor of $\sim$23 at $f=10$ vol% for the optimum nanocomposite parameters. Reproduced with permission from K.M.F. Shahil and A.A. Balandin, *Nano Lett.*, **12**, 861 (2012).

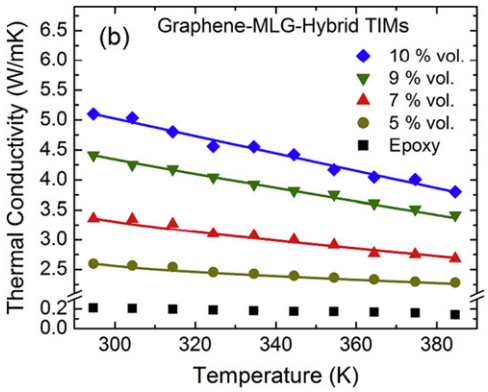

Fig. 6. (Color online) Measured dependence of the thermal conductivity of TIMs on temperature for different loading fractions. The weak temperature dependence is beneficial for applications of the composites as TIMs. Reproduced with permission from K.M.F. Shahil and A.A. Balandin, *Nano Lett.*, **12**, 861 (2012).

Both graphene and CNTs can be regarded as spheroids with principle dimensions $a_1=a_2$ and a_3. An ideal graphene flake can be treated as an oblate spheroid with $\alpha=a_3/a_1\to 0$, while CNT can be treated as a prolate spheroid with $\alpha\to\infty$. This difference in α was theoretically predicted to make graphene much better filler than CNTs [56]. Assuming randomly oriented fillers and incorporating TBR, one can write for MLG composites [54]

$$K = K_p[3K_m + 2f(K_p - K_m)]/[(3-f)K_p + K_m f + R_B K_m K_p f/H]. \quad (1)$$

Here R_B is TBR at the graphene–matrix interface, while K_p and K_m are thermal conductivity of the filler and matrix materials, respectively. Graphene has large phonon mean-free path $\Lambda\sim 775$ nm at RT [1], which is comparable to L. To account for the size effects on heat conduction inside MLG, we altered EMA by introducing $K_p=(1/3)C\upsilon\Lambda_{\text{eff}}$, where $1/\Lambda_{\text{eff}}=1/\Lambda+1/L$, C is the specific heat and υ is the phonon velocity. For simplicity, we assumed $K_p/K_m\sim 1000$ for both MLG and CNTs and took TBR values for CNTs and graphene as $\sim 8.3\times 10^{-8}$ m^2 K/W [33] and $\sim 3.7\times 10^{-9}$ m^2 K/W [57], respectively. The calculations confirmed that MLG can produce higher TCE than CNTs even as one varies α and diameter D of CNTs in a wide range.

The modified EMA was used to extract the actual TBR in the nanocomposite graphene–MLG-epoxy TIMs by fitting the calculated K to the experimental data and varying R_B value. For MLG, we used $\alpha=0.01$ ($\approx H/L$) and assumed $\Lambda=775$ nm [6]. The best match with experiment is attained at $R_B=3.5\times 10^{-9}$ K m^2/W. This value is small, and it is consistent with the molecular dynamics (MD) simulations [57]. Our own calculations indicate that for higher R_B, TCE does not increase with f linearly but starts to saturate. In addition to the geometrical factors, the reduction of TBR at the filler–matrix interface is another key condition for achieving high TCE for graphene–MGL nanocomposite. Recent ab initio density function theory (DFT) and MD study [58] suggested a possibility of extraordinary K enhancement in ordered graphene composites ($K/K_m\approx 360$ at $f\approx 5\%$) due to graphene's planar geometry and strong coupling of the functionalized graphene to the organic molecules with the corresponding decrease in Kapitza resistance. This implies that certain phonon modes excited in graphene and couple well to those in organic molecules and the mismatch in the phonon DOS between graphene–matrix is smaller than between CNT–matrix. The experimental data reported in Ref. [54] are in line with the DFT and MD predictions [57,58].

It follows from our analysis that graphene's geometry ($\alpha\to 0$ in graphene as opposed to $\alpha\to\infty$ in CNTs) and lower Kapitza resistance are the key factors in achieving outstanding TCE. The role of the percolation threshold is not clear yet. Theory suggests that $f_T\sim 1/\alpha$ [35,59], which explains the low electrical percolation f_T for CNTs. This can also indicate that for MLG, f_T should be much larger and heat conduction is assisted, instead, by better graphene and MLG thermal coupling to the matrix. The latter conclusion is supported by the extracted value of R_B and theoretical estimates of Kapitza resistance. These considerations do not exclude attachments of graphene and MLG flakes to each other with good thermal links without forming a completely percolated network. In the examined f range our TIM samples remained electrically insulating with the measured electrical resistivity of $\rho\approx 1.4\times 10^9\ \Omega$ cm.

It has been established from the trial-and-error studies that it is essential to have both graphene and MGL in the nanocomposite for achieving maximum TEC. The single-layer or bilayer graphene have greater flexibility to form the thermal links while K_p in MGL ($n>3$) is subject to less degradation due to phonon boundary scattering [1]. The TIM performance, defined by R_{TIM}, depends not only on K but also on BLT [11–13]. Using an approximated BLT and measured TCE of 2300%, we conservatively estimated that R_{TIM} of the nanocomposite graphene–MLG TIMs should be, at least, on the order of magnitude smaller than that of conventional or CNT based TIMs. The achieved TCE at $f=10\%$ is higher than that in graphite composites [60], GnP–CNT epoxy composites [61–67], graphite nanocomposites [63], or chemically functionalized graphite composites [64] at the same or even higher carbon loading.

In order to evaluate the effectiveness of graphene–MLG-based TIMs in the practical setting of the two proximate surfaces and TIM between them, the thermal conductivity across the thermal contact was also measured. The sandwiches of the two mating surfaces made of aluminum with the TIM in between two surfaces have been prepared for these studies. The initial material was a commercial thermal grease (a type of TIM), which had Al and ZnO_2 particles as the fillers [65]. The thermal conductivity of the stacked metal–grease–metal sandwiches was measured using the same technique. The thermal conductivity of the thermal grease determined in our experiments was ~ 5.8 W/mK, which compares well with the value provided by the vendor. As the next step, we modified the grease by adding a small quantity ($f=2$ vol%) of the mixture of graphene–MLG, and prepared several sandwiches of the metal–TIM–metal. The thermal conductivity of the total structure was measured again following the same procedure. The extracted thermal conductivity of our graphene–MLG–grease TIM was found to be ~ 14 W/mK at RT. This corresponds to K/K_m ratio of ~ 2.4, i.e., TCE factor of ~ 1.4, at the very small 2% loading fraction [54].

For comparison, in the case of our graphene–MLG-epoxy composite the TCE factor is ~ 3 at 2% loading, which corresponds to $K/K_m\sim 4$ (see Fig. 5). Although the TCE factor in the tested commercial grease with graphene is smaller than that in the graphene–epoxy composite, it is still significant. It is reasonable to assume that in the commercial grease the TCE factor is smaller than in the graphene–MLG-epoxy nanocomposites owing to the presence of other filler particles with the relatively low intrinsic K. A different graphene–matrix coupling can also affect the K value. In the graphene–epoxy composites we also start with the much smaller matrix thermal conductivity K_m. A hybrid mixture of graphene–MLG and Al and ZnO_2 can be the efficient filler owing to a complex interactions among different filler particles [14].

It is important to note that by using a small loading fraction, one can keep the viscosity and other important mechanical characteristics, such as conformity, of the original thermal grease unaffected. Conformability allows TIM to fill the microscopic valleys on the surface of the mating surfaces, thus displacing air, which is thermally insulating. The good spreading characteristics allow one to minimize the TIM thickness: the larger thickness would result in the higher thermal resistance. The data in Table 1 confirmed that TCE values achieved in the graphene based TIMs are indeed the highest reported to date. The upper

Table 1
Thermal interface materials with various fillers.

Filler	Properties		Loading	Base material	Measurement	Ref.
	TCE (%)	K (W/mK)				
Part I: Non-carbon fillers						
Ni	566		$<30\%$	Epoxy	Laser flash	[81]
Al_2O_3	–	0.35–0.65	50 wt%	Epoxy	Guarded flow	[89]
ALN	1900		60%	Epoxy	ASTM	[82]
BN	650		30 wt%	Epoxy	ASTM	[83]
Al_2O_3	–	0.18	10 wt%	PS	Laser flash	[84]
BN	–	0.8–1.2	0–35 vol%	Polyethylene	Hot disk	[88]
AlN	–	1.3	40 vol%	Epoxy	Laser flash	[87]
Ag	–	3.0	28 vol%	Epoxy	Laser flash	[85]
Part II: TIM with CNT fillers						
MWNT	150	–	1.0 vol%	Oil	Hot wire	[31]
SWNT	125	–	1.0 wt%	Epoxy	Comparative	[77]
p-SWNT	350		9.0 wt%	Epoxy	Laser flash	[29]
CNT	65		3.8 wt%	Silicone	ASTM	[78]
SWNT	50		1 wt%	Polystyrene	Steady state	[66]
SWNT	55	–	7.0 wt%	PMMA	Guarded plate	[30]
SWNT	–	4.8	–	–	–	[91]
MWNT	–	0.5	–	Epoxy	ASTM	[92]
SWNT	–	0.61	2.3 wt%	Epoxy	Comparative	[90]
MWNT	–	0.43	–	–	ASTM	[93]
MWNT		1.21	–	–	ASTM	[94]
Part III: TIM with graphene, graphite and diamond fillers						
Diamond	$\sim$406	1.2	60 wt%	Epoxy	Laser flash	[86]
Carbon nanofiber	$\sim$945	1.845	40 wt%	Rubbery epoxy	Hot disk	[95]
GnP	3000	–	25.0 vol%	Epoxy	Laser flash	[79]
GON	30–80	–	5.0 vol%	Glycol and paraffin	Comparative	[80]
GnP	10	0.23	1.0 vol%	Epoxy	Hot wire	[76]
GnP	700	1.4	20 wt%	Silicone	Hot disk	[96]
Graphite	1800	–	20 wt%	Epoxy	Laser flash	[60]
GnP	990	1.909	20 wt%	Silicone	Hot disk	[97]
Graphene–MLG	2300	5.1	10 vol%	Epoxy	Laser flash	[54]

part of the table lists TIMs with non-carbon fillers such as metal and boron nitride (BN) micro- and nano-particles. The middle part summarizes data for TIMs filled with CNTs. The lower part of the table provides data for TIMs with graphite, GnP and graphene. For comparison, the data point for diamond is also included.

The large TCE factors are often accompanied by increasing electrical conductivity σ, i.e., decreasing ρ. In our case, we observed a record-high TEC without a substantial change in ρ in the examined f range. The increase of TEC without decreasing ρ was reported in a few other studies. For example, a substantial enhancement of K in the composites with CNTs at 1 wt% loading was reported in Ref. [66]. The electrical conductivity σ of the composites remained low 10^{-11}–10^{-9} S/cm in these samples. The low σ of 10^{-15}–10^{-9} S/cm in the SWNT/PS composites with enhanced K was also reported [67]. Moreover, there were studies where the increasing K was accompanied by the decreasing σ in the composite with the same filler fraction [61].

The increase in the thermal conductivity without substantial change in the electrical conductivity can be explained by the following. The strong increase in the electrical conductivity in the composite with the electrically insulating matrix requires formation of the percolation network. In our case, we have enhancement of K owing to the present of graphene–MLG fillers, perhaps with partial ordering, while the complete percolation network is not formed. The heat can be conducted through the matrix while the electrical current cannot. The narrow layers of the epoxy matrix may not present a substantial thermal resistance while blocking the electric current. According to the theory [35,68], an increase in the thickness of the polymer layer from zero to 10 nm does not affect significantly the heat transport while such an increase in the width of the tunneling barrier for the electrons would effectively eliminate the electrical transport.

6. Thermal boundary resistance at the graphene–matrix interface

Heat conduction across graphene and FLG on substrates was measured by several different techniques, including electrical 3-omega, Raman-electrical, and optical pump-and-probe methods [69–72]. The thermo-reflectance technique was used to study graphite interface with Cr, Al, Ti and Au [73]. The RT TBR of $\sim 10^{-8}$ K m^2/W was found in most of cases. The summary of the reported TBR data is provided in Table 2. The studies, which utilized different experimental techniques, were in agreement that the cross-plane conductance G or TBR do not reveal a strong dependence on the thickness of FGL or nature of the dielectric or metal substrate. TBR decreases with temperature following a typical trend for Kapitza resistance.

The first-principle calculations of heat transfer between graphene and SiO_2, which treated the graphene–substrate coupling as a week van der Waals-type interaction, determined the heat transfer coefficient of $\sim 2.5 \times 10^7$ W/(m^2 K) [74]. This translates to TBR of $\sim 4 \times 10^{-8}$ K m^2/W, which is close to experimental data. Despite agreement on the average TBR, most studies note a significant sample to sample variation in TBR at graphene–SiO_2 interface (e.g., factor of $\sim$4 for FLG with $n=5$ in Ref. [71]). This means that graphene thermal coupling to other materials can depend strongly on the surface roughness, presence or absence of suspended regions in graphene layers, and methods of graphene

Table 2
Thermal boundary resistance.

Interface	Thermal resistance (K m^2/W)	Method	Ref.
Alumina–Polymer	2.5×10^{-8}–5×10^{-8}	3ω method	[98]
CNT–D_2O	8.3×10^{-8}	Transient absorption	[33]
Carbon nanofiber–Cu	0.25×10^{-4}	ASTM	[100]
Aligned MWCNT	$8–18\times10^{-6}$	Photoacoustic technique	[99]
CNT–CNT interface	3.8×10^{-4}	Infrared technique	[101]
Graphene–SiO_2	$\sim4\times10^{-8}$	Raman and electrical	[69]
Graphene–SiO_2	$\sim(0.6–12)\times10^{-8}$	Electrical	[70]
Graphene–SiO_2	$\sim2\times10^{-8}$	Pump and probe	[71]
Metal–graphene–SiO_2	$\sim4\times10^{-8}$	Raman and electrical	[72]
Graphite–metal	$\sim(1–3)\times10^{-8}$	Reflectance	[73]
Graphene/a-SiO_2	$\sim4\times10^{-8}$	Theory	[74]
Graphene–oil	$\sim(0.4–4)\times10^{-8}$	Theory	[57]
Graphene–epoxy	$\sim3.5\times10^{-9}$	Laser flash	[54]

preparation. The low TBR of graphene with many materials add validity to the proposed graphene and MLG applications in TIMs.

7. Hybrid graphene–metal nano/micro-particle composites

In this section we describe recent progress in the electrically conductive TIMs achieved via a combination of graphene and MLG with metal nano- and micro-particles in hybrid composites. We follow the methods and data reported in Ref. [75]. For this study, the authors used electrically conductive silver epoxy with the silver particles as the initial filler. The sizes of the silver particles were in micrometer range. The graphene–FLG solution was prepared by the flake isolation via the density gradient ultra-centrifugation (DGU) [23]. The aqueous-solution-phase approach was enabled by the sodium cholate (SC) surfactant [24]. In DGU, the solution of graphite flakes is centrifuged to control the MLG thickness. To remove the thick graphite material from the dispersion, the centrifugation was performed at 15k rpm for 5 min. The final product was encapsulated graphene–MLG sheets with the concentration of ~0.05 mg/mL. The utilized liquid graphene–MLG solution had the single layer graphene and bilayer graphene content of ~27% and 48%, respectively. The solution was treated thermally to reduce the surfactant concentration and improve the flake-to-flake contact.

The hybrid graphene–metal-epoxy composites were prepared by dispersing the graphene solution in the silver epoxy, and applying the high-shear mixing with the following ultrasonication. The epoxy hardener was added to the homogeneous mixture of the graphene–silver epoxy and shear mixed. Fig. 7(a) shows the scanning electron microscopy (SEM) image of the resulting hybrid graphene–silver-epoxy composite. One can see the silver particles as the μm-scale grains. The graphene–MLG flakes with nm-scale thickness and lateral sizes varying from nm to μm scale are more difficult to distinguish. Their presence and concentration were verified with the electron dispersive spectroscopy (EDS). The EDS data presented in Fig. 7(b) reveals carbon (C) atoms present together with silver (Ag) and oxygen (O) atoms. The left inset to Fig. 7(b) is the TEM image of MLG flakes utilized in the composite. The selected-area electron-diffraction patterns, collected during TEM characterization, indicated that graphene flakes retained their good crystal structure after all processing steps. The right inset to Fig. 7(b) shows the image of the TIM sample.

Fig. 8 presents the measured thermal conductivity of the commercial silver epoxy, the hybrid composites with different graphene–MLG loading and reference composites with the carbon black. The error bars represent the data scatter for several samples. The measured K for the commercial silver-epoxy TIM was 1.67 W/mK, which is in agreement with the value provided

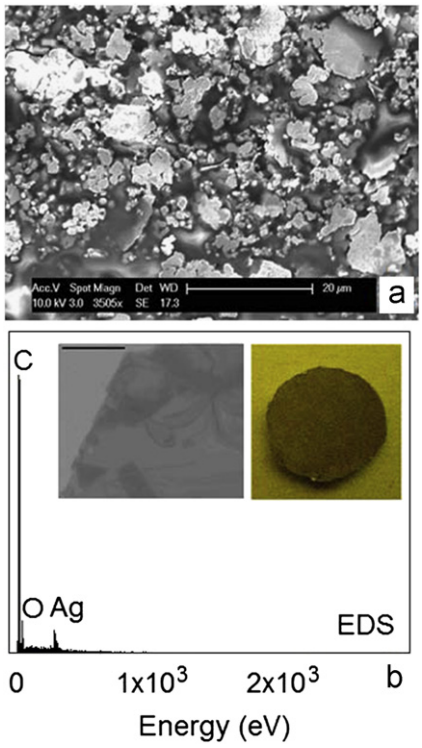

Fig. 7. (Color online) (a) SEM image of the graphene–silver-epoxy composite. (b) EDS data for the composites indicating the presence and concentration of graphene–FLG particles together with the silver particles. The left inset shows TEM image of a representative graphene flake used in the composites. The scale bar is 25 nm. The right inset shows an optical image of TIM sample prepared for thermal measurements. The diameter of the sample is 10 mm and its thickness is 1 mm. Reproduced with permission from V. Goyal and A.A. Balandin, *Appl. Phys. Lett.*, **100**, 073113 (2012).

by the vendor. The thermal conductivity of the reference composite does not increase noticeably with the addition of carbon black in the examined f range. Carbon black is an amorphous material with low K [1]. However, one can see a drastic K increase in the composites with addition of the graphene–FLG filler. The RT thermal conductivity of TIMs with the graphene–FLG nano-micro-filler particles reaches ~9.9 W/mK at the small 5 vol% of the graphene–FLG loading. This is significant increase by a factor of ~6, which corresponds to ~500% K enhancement as compared to the commercial silver-epoxy TIM.

The epoxy matrix is a weak conductor of heat and electrical insulator. However, the high loading fraction of silver particles in the pristine silver epoxy ensures that TIM is electrically conductive.

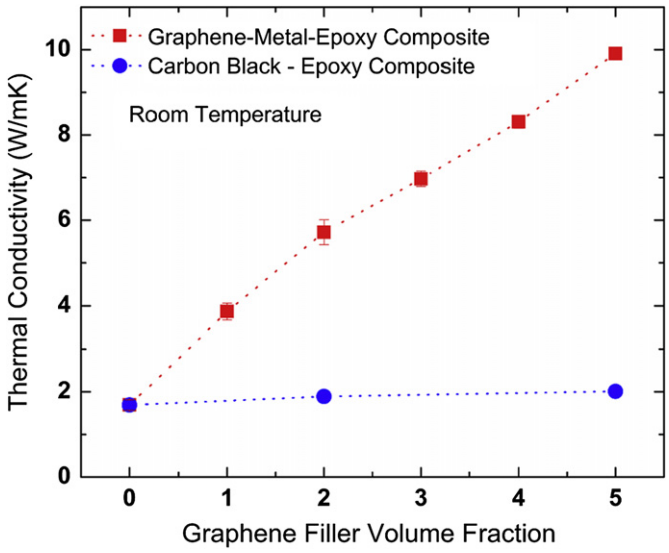

Fig. 8. (Color online) Thermal conductivity of the pristine silver epoxy, hybrid graphene–FLG–silver-epoxy composites and the reference silver epoxy–carbon black composites as a function of the volume fraction f of the graphene–FLG nano-micro-filler. Reproduced with permission from V. Goyal and A.A. Balandin, *Appl. Phys. Lett.*, **100**, 073113 (2012).

The measurements of the silver epoxy revealed the electrical resistivity $\rho_e \approx 10^{-4}\,\Omega$ m. The low ρ_e means that the silver particles touch each other forming an electrically percolating network. It is interesting to note that ρ_e of the hybrid samples did not change noticeably with addition of graphene. The latter can be explained by the fact that since the composite is highly electrically conductive by itself the addition of only 5 vol% of graphene–MLG cannot change its ρ substantially.

8. Conclusions

We reviewed the thermal properties of graphene and discussed applications of graphene and MLG in thermal interface materials. It was pointed out that one can obtain the thermal conductivity enhancement by a factor of $\sim$23 with the help of graphene–MLG at f=10% loading, which is higher than anything reported to-date. The unusual enhancement was explained by high intrinsic K_i of graphene and MLG; low Kapitza resistance at the graphene–matrix interface; geometrical shape of graphene–MLG flakes ($a \to 0$); high flexibility if MLG ($n < 5$); and the optimum mix of graphene and MGL with different thickness and lateral size. Additional benefits of the graphene-based composites, which come at no additional expense, are their low coefficient of thermal expansion and increased mechanical strength. It has also been shown that one can obtained the thermal conductivity of $\sim$14 W/mK in the commercial thermal grease via addition of only f=2% of the optimized graphene–MLG mixture. The graphene-based TIMs have the thermal resistance reduced by orders-of-magnitude and be can produced inexpensively on an industrial scale.

Acknowledgements

This work was supported, in part, by the Office of Naval Research (ONR) through award N00014-10-1-0224 on graphene heat spreaders and by the Semiconductor Research Corporation (SRC) and Defense Advanced Research Project Agency (DARPA) through FCRP Center on Functional Engineered Nano Architectonics (FENA). A.A.B. acknowledges UC Discovery grant on TIM applications in solar cells. The authors acknowledge useful discussions on TIMs with Intel Corporation engineers and the former members of the Nano-Device Laboratory (NDL)—Dr. S. Ghosh (Intel), Dr. D. Teweldebrhan (Intel) and Dr. V. Goyal (Texas Instrument).

References

[1] A.A. Balandin, Nat. Mater. 10 (2011) 569–581.
[2] A.C. Ferrari, J.C. Meyer, V. Scardaci, C. Casiraghi, M. Lazzeri, F. Mauri, S. Piscanec, D. Jiang, K.S. Novoselov, S. Roth, A.K. Geim, Phys. Rev. Lett. 97 (2006) 187401.
[3] I. Calizo, A.A. Balandin, W. Bao, F. Miao, C.N. Lau, Nano Lett. 7 (2007) 2645.
[4] I. Calizo, F. Miao, W. Bao, C.N. Lau, A.A. Balandin, Appl. Phys. Lett. 91 (2007) 071913.
[5] I. Calizo, W. Bao, F. Miao, C.N. Lau, A.A. Balandin, Appl. Phys. Lett. 91 (2007) 201904.
[6] I. Calizo, I. Bejenari, M. Rahman, G. Liu, A.A. Balandin, J. Appl. Phys. 106 (2009) 043509.
[7] D. Teweldebrhan, A.A. Balandin, Appl. Phys. Lett. 94 (2009) 013101.
[8] D.L. Nika and A.A. Balandin, J. Phys. Condens. Matter, (2012), 〈arXiv:1203.4282〉.
[9] A. Balandin, IEEE Spectr. 29 (2009) 35–39.
[10] S.V. Garimella, A.S. Fleischer, J.Y. Murthy, A. Keshavarzi, R. Prasher, C. Patel, S.H. Bhavnani, R. Venkatasubramanian, R. Mahajan, Y. Joshi, B. Sammakia, B.A. Myers, L. Chorosinski, M. Baelmans, P. Sathyamurthy, P.E. Raad, IEEE Trans. Compon. Packag. Technol. 31 (2008) 801–815.
[11] R. Prasher, Proc. IEEE 94 (2006) 1571–1585.
[12] F. Sarvar, D.C. Whalley and P.P. Conway, Proceedings of the Electronics System Integration Technology Conference (IEEE 1-4244-0553) 2, 2006, pp. 1292–1302.
[13] R.S. Prasher, J.Y. Chang, I. Sauciuc, S. Narasimhan, D. Chau, G. Chrysler, A. Myers, S. Prstic, C. Hu, Intel Technol. J. 9 (2005) 285–296.
[14] J. Felba, Thermally conductive nanocomposites, in: C.P. Wong, K.-S. Moon, Y. Li (Eds.), Nano-Bio-Electronic, Photonic and MEMS Packaging, Springer Science, 2010, pp. 277–314, http://dx.doi.org/10.1007/978.
[15] E. Van Dyk, E. Meyer, A. Leitch, B. Scott, S. Afr. J. Sci. 96 (4) (2000) 198–200.
[16] S. Schuller, P. Schilinsky, J. Hauch, C. Brabec, Appl. Phys. A 79 (2004) 37–40.
[17] X.C. Tong, Advanced materials for thermal management of electronic packaging, Springer Ser. Adv. Microelectron. 30 (2011).
[18] B.J. Brinkworth, M. Sandberg, Sol. Energy 80 (2006) 89–103.
[19] G. Notton, C. Cristofari, M. Mattei, P. Poggi, Appl. Therm. Eng. 25 (2005) 2854–2877.
[20] B. Siegal, Proceedings of SEMI-THERM 26, San Jose, CA, February 2010.
[21] K.S. Novoselov, A.K. Geim, S.V. Morozov, D. Jiang, Y. Zhang, S.V. Dubonos, I.V. Grigorieva, A.A. Firsov, Science 306 (5696) (2004) 666–669.
[22] Y. Hernandez, V. Nicolosi, M. Lotya, F.M. Blighe, Z. Sun, S. De, I.T. McGovern, B. Holland, M. Byrne, Y.K. GunKo, J.J. Boland, P. Niraj, G. Duesberg, S. Krishnamurthy, R. Goodhue, J. Hutchison, V. Scardaci, A.C. Ferrari, J.N. Coleman, Nat. Nanotechnol. 3 (2008) 563–568.
[23] A.A. Green, M.C. Hersam, Nano Lett. 9 (12) (2009) 4031–4036.
[24] M. Lotya, Y. Hernandez, P.J. King, R.J. Smith, V. Nicolosi, L.S. Karlsson, F.M. Blighe, S. De, Z. Wang, I.T. McGovern, G.S. Duesberg, J.N. Coleman, J. Am. Chem. Soc. 131 (10) (2009) 3611–3620.
[25] R. Mahajan, C.P. Chiu, G. Chrysler, Proc. IEEE 94 (7) (Jul. 2006).
[26] A. Watwe and R. Prasher, Presented at the 2001 ASME International Mechanical Engineering Congress and Exposition, New York, paper 2-16-7-5, 2001.
[27] P. Kim, L. Shi, A. Majumdar, P.L. McEuen, Phys. Rev. Lett. 87 (2001) 215502–215504.
[28] E. Pop, D. Mann, Q. Wang, K. Goodson, H. Dai, Nano Lett. 6 (1) (2006) 96–100.
[29] A. Yu, M.E. Itkis, E. Bekyarova, R.C. Haddon, Appl. Phys. Lett. 89 (2006) 133102.
[30] P. Bonnet, D. Sireude, B. Garnier, O. Chauvet, Appl. Phys. Lett. 91 (2007) 201910.
[31] S.U.S. Choi, Z.G. Zhang, W. Yu, F.E. Lockwood, E.A. Grulke, Appl. Phys. Lett. 79 (2001) 2252.
[32] A. Moisala, Q. Lia, I.A. Kinlocha, A.H. Windle, Compos. Sci. Technol. 66 (10) (2006) 1285–1288.
[33] S. Huxtable, D.G. Cahill, S. Shenogin, L. Xue, R. Ozisik, P. Barone, M. Usrey, M.S. Strano, G. Siddons, M. Shim, P. Keblinski, Nat. Mater. 2 (2003) 731.
[34] P.L. Kapitza, J. Phys. USSR 4 (1941) 181.
[35] N. Shenogina, S. Shenogin, L. Xue, P. Keblinski, Appl. Phys. Lett. 87 (2005) 133106.
[36] A.A. Balandin, S. Ghosh, W. Bao, I. Calizo, D. Teweldebrhan, F. Miao, C.N. Lau, Nano Lett. 8 (3) (2008) 902–907.
[37] D.L. Nika, E.P. Pokatilov, A.S. Askerov, A.A. Balandin, Phys. Rev. B 79 (2009) 155413.
[38] S. Ghosh, W. Bao, D.L. Nika, S. Subrina, E.P. Pokatilov, C.N. Lau, A.A. Balandin, Nat. Mater. 9 (2010) 555–558.
[39] S. Ghosh, I. Calizo, D. Teweldebrhan, E.P. Pokatilov, D.L. Nika, A.A. Balandin, W. Bao, F. Miao, C.N. Lau, Appl. Phys. Lett. 92 (2008) 151911–151913.

[40] S. Ghosh, D.L. Nika, E.P. Pokatilov, A.A. Balandin, New J. Phys. 11 (095012) (2009) 1–18.
[41] W. Cai, A.L. Moore, Y. Zhu, X. Li, S. Chen, L. Shi, R.S. Ruoff, Nano Lett. 10 (2010) 1645–1651.
[42] K.F. Mak, J. Shan, T.F. Heinz, Phys. Rev. Lett. 106 (2011) 046401.
[43] L.A. Jauregui, Y. Yue, A.N. Sidorov, J. Hu, Q. Yu, G. Lopez, R. Jalilian, D.K. Benjamin, D.A. Delk, W. Wu, Z. Liu, X. Wang, Z. Jiang, X. Ruan, J. Bao, S.S. Pei, Y.P. Chen, ECS Trans. 28 (5) (2010) 73–83.
[44] J.H. Seol, I. Jo, A.L. Moore, L. Lindsay, Z.H. Aitken, M.T. Pettes, X. Li, Z. Yao, R. Huang, D. Broido, N. Mingo, R.S. Ruoff, L. Shi, Science 328 (5975) (2010) 213–216.
[45] P. Blake, P.D. Brimicombe, R.R. Nair, T.J. Booth, D. Jiang, F. Schedin, L.A. Ponomarenko, S.V. Morozov, H.F. Gleeson, E.W. Hill, A.K. Geim, K.S. Novoselov, Nano Lett. 8 (6) (2008) 1704–1708.
[46] K.S. Kim, Y. Zhao, H. Jang, S.Y. Lee, J.M. Kim, K.S. Kim, J.H. Ahn, P. Kim, J.Y. Choi, B.H. Hong, Nature 457 (7230) (2009) 706–710.
[47] X.L. Li, G.Y. Zhang, X.D. Bai, X.M. Sun, X.R. Wang, E. Wang, H.J. Dai, Nat. Nanotechnol. 3 (9) (2008) 538–542.
[48] R.S. Ruoff, J. Mater. Chem. 21 (2011). 3272-3272.
[49] S.Y. Bae, I.-Y. Jeon, J. Yang, N. Park, H.S. Shin, S. Park, R.S. Ruoff, L. Dai, J.-B. Baek, ACS Nano 5 (2011) 4974–4980.
[50] X.S. Li, C.W. Magnuson, A. Venugopal, R.M. Tromp, J.B. Hannon, E.M. Vogel, L. Colombo, R.S. Ruoff, J. Am. Chem. Soc. 133 (2011) 2816–2819.
[51] X.S. Li, C.W. Magnuson, A. Venugopal, J. An, J.W. Suk, B. Han, M. Borysiak, W. Cai, A. Velamakanni, Y. Zhu, L. Fu, E.M. Vogel, E. Voelk, L. Colombo, R.S. Ruoff, Nano Lett. 10 (2010) 4328–4334.
[52] S. Stankovich, D.A. Dikin, G.H.B. Dommett, K.M. Kohlhaas, E.J. Zimney, E.A. Stach, R.D. Piner, S.T. Nguyen, R.S. Ruoff, Nature 442 (2006) 282–286.
[53] D. Li, M.B. Müller, S. Gilje, R.B. Kaner, G.G. Wallace, Nat. Nanotechnol. 3 (2008) 101–105.
[54] K.M.F. Shahil, A.A. Balandin, Nano Lett. 12 (2012) 861.
[55] C.W. Nan, R. Birringer, D.R. Clarke, H. Gleiter, J. Appl. Phys. 81 (1997) 6692.
[56] S.H. Xie, Y.Y. Liu, J.Y. Li, Appl. Phys. Lett. 92 (2008) 243121.
[57] D. Konatham, A. Striolo, Appl. Phys. Lett. 95 (2009) 163105.
[58] D. Konatham, K.N.D. Bui, D.V. Papavassiliou, A. Striolo, Mol. Phys. 109 (1) (2011) 97–111.
[59] P. Keblinski, F. Cleri, Phys. Rev. B 69 (2004) 184201.
[60] B. Debelak, K. Lafdi, Carbon 45 (2007) 1727.
[61] A. Yu, P. Ramesh, X. Sun, E. Bekyarova, M.E. Itkis, R.C. Haddon, Adv. Mater. 20 (2008) 4740.
[62] C. Lin, D.D.L. Chung, Carbon 47 (2009) 295.
[63] H. Fukushima, L.T. Drzal, B.P. Rook, M.J. Rich, Therm. Anal. Calorim. 85 (2006) 235.
[64] S. Gangui, A.K. Roy, D.P. Anderson, Carbon 46 (2008) 806.
[65] S. Narumanchi, M. Mihalic, K. Kelly and G. Eesley, Itherm-2008, NREL/CP-540-42972, FL, USA, May 2008.
[66] M.B. Jakubinek, M.A. White, M. Mu, K.I. Winey, Appl. Phys. Lett. 96 (2010) 083105.
[67] M.N. Tchoul, W.T. Ford, M.L.P. Ha, I.C. Sumarriva, B.P. Grady, G. Lolli, D.E. Resasco, S. Arepalli, Chem. Mater. 20 (2008) 3120.
[68] S. Shenogin, L.P. Xue, R. Ozisik, P. Keblinski, D.G. Cahill, J. Appl. Phys. 95 (2004) 8136.
[69] M. Freitag, M. Steiner, Y. Martin, V. Perebeinos, Z. Chen, J.C. Tsang, P. Avouris, Nano Lett. 9 (2009) 1883–1888.
[70] Z. Chen, W. Jang, W. Bao, C.N. Lau, C. Dames, Appl. Phys. Lett. 95 (2009) 161910–161913.
[71] K.F. Mak, C.H. Liu and T.F. Heinz, Thermal conductance at the graphene–SiO_2 interface measured by optical pump–probe spectroscopy. 〈arXiv:1009.0231〉, 1–10 (2010).
[72] Y.K. Koh, M.H. Bae, D.G. Cahill, E. Pop, Nano Lett. 10 (2010) 4363–4368.
[73] A.J. Schmidt, K.C. Collins, A.J. Minnich, G. Chen, J. Appl. Phys. 107 (2010). 104907-5.
[74] B.N.J. Persson, H. Ueba, Europhys. Lett. 91 (2010) 56001–56005.
[75] V. Goyal, A.A. Balandin, Appl. Phys. Lett. 100 (2012) 073113.
[76] M.T. Hung, O. Choi, Y.S. Ju, H.T. Hahn, Appl. Phys. Lett. 89 (2006) 023117.
[77] M.J. Biercuk, M.C. Laguno, M. Radosavljevic, J.K. Hyun, A.T. Johnson, E.J. Fischer, Appl. Phys. Lett. 80 (2002) 2767.
[78] C.H. Liu, H. Huang, Y. Wu, S.S. Fan, Appl. Phys. Lett. 84 (2004) 4248.
[79] A. Yu, P. Ramesh, M.E. Itkis, E. Bekyarova, R.C. Haddon, J. Phys. Chem. Lett. 111 (2007) 7565.
[80] W. Yu, H. Xie, W. Chen, J. Appl. Phys. 107 (2010) 094317.
[81] S. Nikkeshi, M. Kudo, T. Masuko, J. Appl. Polym. Sci. 69 (1998) 2593.
[82] M. Ohashi, S. Kawakami, Y. Yokogawa, G.C. Lai, J. Am. Ceram. Soc. 88 (2005) 2615.
[83] M.J. Hodgin and R.H. Estes, Proceedings of the National Electronic Packaging and Production Conference, 359, 1999.
[84] H. Dong, L. Fan, C.P. Wong, Proc. Electron. Compon. Technol. Conf. 55 (2) (2005) 1451–1454.
[85] R.C. Campbell, S.E. Smith and R.L. Dietz Annual IEEE Semiconductor Thermal Measurement and Management Symposium 15, San Diego, CA, USA, 1999, pp. 83–97.
[86] W.S. Lee, J. Yu, Diamond Relat. Mater. 14 (10) (2005) 1647–1653.
[87] Y. Xu, D.D.L. Chung, C. Mroz, Composites Part A 32 (12) (2001) 1749–1757.
[88] W. Zhou, S. Qi, H. Li, S. Shao, Thermochim. Acta 452 (1) (2007) 36–42.
[89] L. Fan, B. Su, J. Qu, C.P. Wong, Proc. Electron. Compon. Conf. 54 (1) (2004) 148–154.
[90] F. Du, C. Guthy, T. Kashiwagi, J.E. Fischer, K.I. Winey, J. Polym. Sci., Part B: Polym. Phys. 44 (10) (2006) 1513–1519.
[91] T.M. Lee, K.C. Chiou, F.P. Tseng, C.C. Huang, Proc. Electron. Compon. Conf. 55 (2005) 55–59.
[92] K. Zhang, G.W. Xiao, C.K.Y. Wong, H.W. Gu, M.M.F. Yuen, P.C.H. Chan, B. Xu, Proc. Electron. Compon. Conf. 55 (2005) 60–65.
[93] Y. Wu, C.H. Liu, H. Huang, S.S. Fan, Appl. Phys. Lett. 87 (21) (2005) 1.
Y. Wu, C.H. Liu, H. Huang, S.S. Fan, Solid State Phenom. 121–123 (2007) 243.
[94] H. Huang, C. .H. Liu, Y. Wu, S. Fan, Adv. Mater. 17 (13) (2005) 1652.
[95] M.A. Raza, A. Westwood, C. Stirling, Carbon 50 (1) (2012) 84–97.
[96] M.A. Raza, A.V.K. Westwood, C. Stirling, International Symposium on Advanced Packaging Materials, Microtech, Cambridge, 2010 34 –48.
[97] M.A. Raza, A. Westwood, A. Brown, N. Hondow, C. Stirling, Carbon 49 (13) (2011) 4269.
[98] S.A. Putnam, D.G. Cahill, B.J. Ash, L.S. Schadler, J. Appl. Phys. 94 (10) (2003) 6785–6788.
[99] P.B. Amama, B.A. Cola, T.D. Sands, X. Xu, T.S. Fishe, Nanotechnology 18 (38) (2007) 385303.
[100] Q. Ngo, B.A. Cruden, A.M. Cassell, G. Sims, M. Meyyappan, J. Li, C.Y. Yang, Nano Lett. 4 (12) (2004) 2403–2407.
[101] X.J. Hu, M.A. Panzer, K.E. Goodson, J. Heat Transfer 129 (1) (2007) 91.